

Article

Unraveling FeO_x Nanoparticles Confined on Fibrous Mesoporous Silica Catalyst Construction and CO Catalytic Oxidation Performance

Guobo Li ^{1,†}, Weiwei Feng ^{1,†}, Yiwei Luo ¹, Jie Yan ¹ , Yining Cai ¹, Yiling Wang ¹, Shule Zhang ², Wenming Liu ³ and Honggen Peng ^{1,*} 

¹ School of Resources and Environment, Nanchang University, Nanchang 330031, China; liguobo@ncu.edu.cn (G.L.); fengweiwei@email.ncu.edu.cn (W.F.); lyw243757814@163.com (Y.L.); 19914754363@163.com (J.Y.); 5811121108@email.ncu.edu.cn (Y.C.); wangyilin312@outlook.com (Y.W.)

² School of Chemical Engineering, Nanjing University of Science and Technology, Nanjing 210094, China; shulezhang@163.com

³ School of Chemistry and Chemical Engineering, Nanchang University, Nanchang 330031, China; wmliu@ncu.edu.cn

* Correspondence: penghonggen@ncu.edu.cn; Tel.: +86-0791-8396-9583

† These authors contributed equally to this work.

Abstract: Catalytic oxidation is used to control carbon monoxide (CO) emissions from industrial exhaust. In this study, a mesoporous silica material, KCC-1, was synthesized and used as a carrier with a high specific surface area to confine active component FeO_x nanoparticles (NPs), and the CO catalytic oxidation performance of x%Fe@KCC-1 catalysts (x represents the mass loading of Fe) was studied. The experimental results showed that due to its large specific surface area and abundant mesopores, the FeO_x NPs were highly dispersed on the surface of the KCC-1 carrier. The particle size of FeO_x was very small, resulting in strong interactions between FeO_x NPs and KCC-1, which enhanced the catalytic oxidation reaction on the catalyst. The FeO_x loading improved the CO adsorption capability of the catalyst, which facilitated the catalytic oxidation of CO, with the 7%Fe@KCC-1 catalyst achieving 100% CO conversion at 160 °C. The CO catalytic removal mechanism was investigated by a combination of in-situ DRIFTS and DFT calculations. This study advances scientific understanding of the application potential of nano-catalysts in important oxidation reactions and provides valuable insights into the development of efficient CO oxidation catalysts.

Keywords: porous catalysts; FeO_x nanoparticles; density functional theory; catalytic removal mechanism



Citation: Li, G.; Feng, W.; Luo, Y.; Yan, J.; Cai, Y.; Wang, Y.; Zhang, S.; Liu, W.; Peng, H. Unraveling FeO_x Nanoparticles Confined on Fibrous Mesoporous Silica Catalyst Construction and CO Catalytic Oxidation Performance. *Catalysts* **2024**, *14*, 63. <https://doi.org/10.3390/catal14010063>

Academic Editor: Patrick Da Costa

Received: 28 November 2023

Revised: 10 January 2024

Accepted: 13 January 2024

Published: 14 January 2024



Copyright: © 2024 by the authors. Licensee MDPI, Basel, Switzerland. This article is an open access article distributed under the terms and conditions of the Creative Commons Attribution (CC BY) license (<https://creativecommons.org/licenses/by/4.0/>).

1. Introduction

Carbon monoxide (CO) is one of the most high-priority pollutants in China's environmental air quality standards. Vehicle exhaust emissions are one of the primary sources of urban air pollution and include CO, nitrogen oxides (NO_x), volatile organic compounds (VOCs), and particulate matters (PMs), all of which [1,2] pose risks to human health and the environment [3]. The preferred method of removing CO from the exhaust gas of diesel vehicles is generally through catalytic oxidation of the CO using a three-way catalyst. Currently, catalytic oxidation of CO using molecular O₂ as an oxidant (2CO + O₂ → 2CO₂) is recognized as the most energy-efficient method of CO removal. Furthermore, as a typical gas-solid heterogeneous reaction, catalytic oxidation of CO is regarded as an extremely important topic for fundamental research. CO can be used as a probe molecule to investigate catalyst structures, adsorption/desorption behaviors, metal-support interactions, and catalytic reaction mechanisms. Extensive efforts have been made in recent years to develop efficient catalysts for CO oxidation. Supported catalysts have received particular attention due to their enhanced catalytic activity, stability, and selectivity [4]. In this regard,

KCC-1, a mesoporous silica material (KCC-1) with an imidazolate ligand, has emerged as a promising support for various catalysts.

KCC-1 possesses a range of desirable properties, including a high surface area, ordered porosity, and thermal stability [5,6]. These characteristics make it an attractive platform for the immobilization of catalytically active species, such as metal oxides. Moreover, the structural and textural tunability of KCC-1 allows for precise control over the dispersion and accessibility of active sites, which influences its overall catalytic performance. Previously, we found that $\text{Sn}_x/\text{KCC-1}$ catalysts with well-dispersed Sn atom clustering exhibited CO catalytic oxidation performance comparable to that of noble metal catalysts [7].

Noble metals, particularly platinum and gold, conventionally serve as pivotal components in catalytic systems for controlling carbon monoxide (CO) emissions via catalytic oxidation [8–10]. Although noble metal catalysts have excellent CO adsorption and activation capacity, they are dwindling and expensive resources. The non-noble metal catalyst FeO_x has shown remarkable catalytic activity for CO oxidation due to its unique redox behavior and high affinity for CO. Liu et al. [11] investigated the overlay adsorption of CO on a Pt (111) surface partially covered by FeO_x nanostructures and showed that FeO_x nanostructures are ideal catalysts for low temperature CO oxidation. The coverage structure of carbon monoxide on bare platinum is unaffected by FeO_x NPs due to strong chemisorption. The incorporation of FeO_x species onto a KCC-1 support can further enhance its catalytic properties by providing a highly dispersed and stabilized active phase. The structural features, surface chemistry, and interactions between FeO_x and KCC-1 are expected to play crucial roles in governing the catalytic performance and stability of supported catalysts. Bai et al. [12] found that Fe-KCC-1 has a large surface area ($464.56 \text{ m}^2 \cdot \text{g}^{-1}$) and that FeO_x NPs particles are well-dispersed on its surface.

Despite increasing interest in utilizing KCC-1 as a FeO_x catalyst carrier, there is still a need to comprehensively investigate the synthesis methods, characterization techniques, and catalytic mechanisms of these composites for CO oxidation. Understanding the structural and electronic properties of the catalyst and the nature of active sites will help elucidate the underlying catalytic mechanism to optimize the design of highly efficient catalysts. The utilization of a confinement strategy proves highly effective in minimizing the sintering of active component NPs, leading to a noteworthy enhancement in catalytic stability. However, conventional confinement techniques, such as porous structures or core shell arrangements, may hinder the transport of reactants to some extent or compromise certain active sites [13–16].

In this study, we synthesized and characterized KCC-1-supported FeO_x catalysts for CO oxidation. By employing various characterization techniques, including X-ray diffraction (XRD), scanning electron microscope (SEM), and HRTEM, we probed the structural integrity, textural properties, dispersion, and oxidation state of FeO_x on the KCC-1 carrier. In addition, catalytic activity measurements were carried out to assess the $x\% \text{Fe@KCC-1}$ ($x = 0, 1, 3, 5, 7$ and 10) catalyst's performance for CO oxidation. The insights gained from this research will provide a fundamental understanding of the KCC-1-supported FeO_x catalyst system, especially the synergistic effects between the support and active species. This knowledge can pave the way for the rational design and synthesis of high-performance catalysts for CO oxidation, leading to air quality improvements and sustainable development.

2. Discussion

2.1. Basic Morphological Characteristics

The morphology and pore structure of catalyst materials play crucial roles in heterogeneous catalysis. SEM images of $x\% \text{Fe@KCC-1}$ ($x = 0, 1, 3, 5, 7$ and 10) catalysts are shown in Figure 1. This series of $x\% \text{Fe@KCC-1}$ catalysts exhibited similar geomorphic features, all of which were hydrangea-like. These features facilitate heterogeneous catalytic reactions on the $x\% \text{Fe@KCC-1}$ ($x = 0, 1, 3, 5, 7$ and 10) catalyst's surface. The overall morphology of the catalysts was unaffected before and after loading the $x\% \text{Fe}$ active component, suggesting that it was well-dispersed on the KCC-1 carrier surface, thus providing abundant active sites.

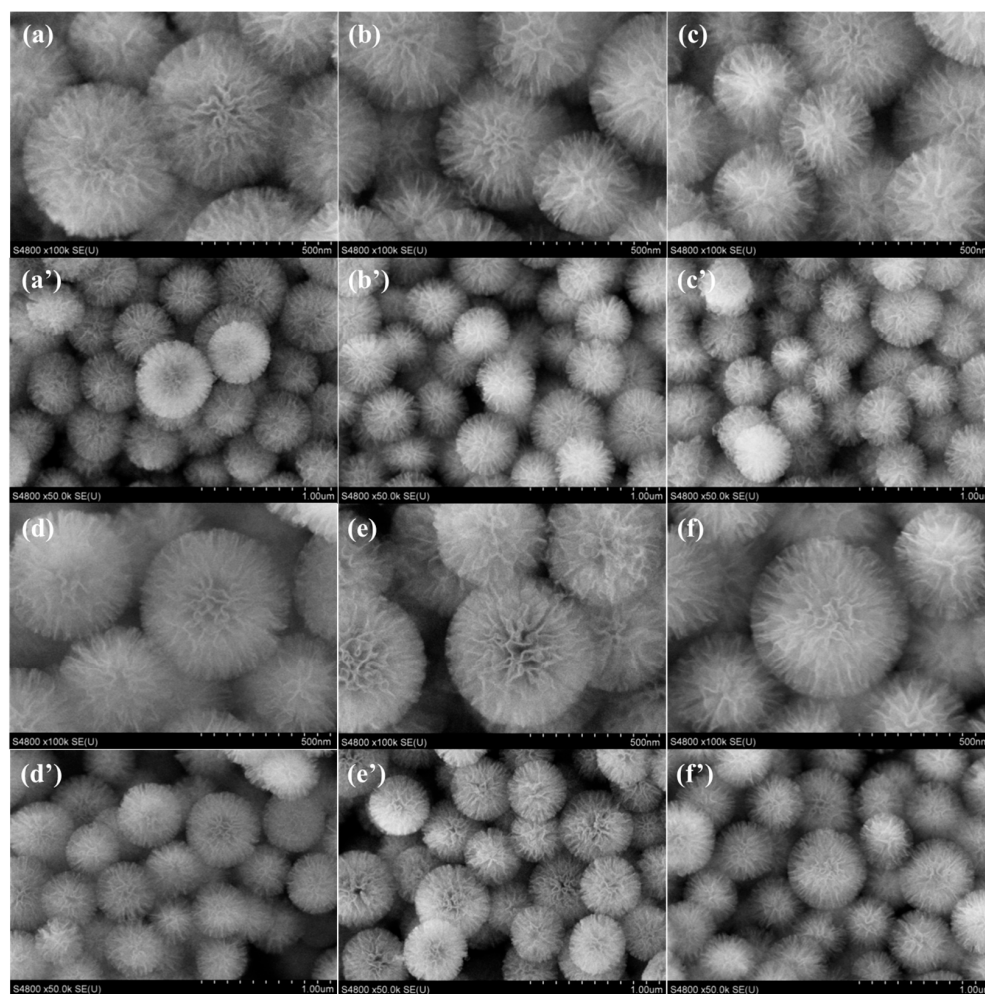


Figure 1. SEM images of (a,a') KCC-1, (b,b') 1%Fe@KCC-1, (c,c') 3%Fe@KCC-1, (d,d') 5%Fe@KCC-1, (e,e') 7%Fe@KCC-1 and (f,f') 10%Fe@KCC-1 catalysts.

The unique lattice structures of KCC-1, FeO_x , and Fe were not detected in the HRTEM of the 7%Fe@KCC-1 catalyst (Figure S1a,b), and were reduced in the 7%Fe@KCC-1 catalyst by H_2 (Figure S2a–d). The mesoporous KCC-1 exhibits a unique fibrous structure (hydrangea-like fibrous microspheres), which suggests that the active components of FeO_x NPs are uniformly dispersed on the surface of the KCC-1 carrier. This homogeneous dispersion effectively ensures the effective collision and interaction between the active components on the catalyst surface and the reactive gas molecules (CO and O_2). In addition, the results of high-angle annular dark-field scanning transmission electron microscopy and energy-dispersive X-ray spectroscopy (Figure S1c–f) showed that the FeO_x active component NPs were uniformly distributed on the KCC-1 without aggregation. This structure allows the FeO_x NPs' active components to be supported on the surface of the fiber structure rather than in the pores, resulting in smaller particle sizes, which is an advantage of KCC-1 molecular sieves. Therefore, the $x\%\text{Fe@KCC-1}$ ($x = 0, 1, 3, 5, 7$ and 10) catalyst is expected to exhibit excellent CO catalytic activity.

The crystal structures of the $x\%\text{Fe@KCC-1}$ ($x = 0, 1, 3, 5, 7$ and 10) catalysts were characterized by XRD, and the obtained pattern is displayed in Figure S3. For the Fe_2O_3 catalyst samples, strong diffraction peaks appeared at 24.25° , 33.25° , 35.72° , 40.94° , 49.55° , 54.12° , 57.69° , 62.52° , 64.08° , and 72.01° , which corresponded to the (0 1 2), (1 0 4), (1 1 0), (1 1 3), (0 2 4), (1 1 6), (0 1 8), (2 1 4), (3 0 0), and (1 0 10) planes of $\alpha\text{-Fe}_2\text{O}_3$ (JCPDS card: 1–089–0597), respectively [17]. Furthermore, the $x\%\text{Fe@KCC-1}$ catalysts showed a broad diffraction peak at $2\theta = 22.58$, which was attributed to amorphous SiO_2 .

within the mesoporous molecular sieve of the KCC-1 [18]. This is an indication that the FeO_x NPs' active component was present on the surface of the KCC-1 in an amorphous form, even with the highest Fe loading, namely that of the 10%Fe@KCC-1 catalyst. Thus, the $x\%\text{Fe@KCC-1}$ ($x = 0, 1, 3, 5, 7$ and 10) catalysts may have excellent heterogeneous catalytic properties.

Nitrogen (N_2) adsorption–desorption isotherms were used to probe the specific surface area and pore structure data of $x\%\text{Fe@KCC-1}$ ($x = 0, 1, 3, 5, 7$ and 10) and related catalyst materials. The resulting N_2 adsorption and desorption isotherms and corresponding BJH pore size distribution curves for the relative pressure (P/P_0) range of 0.05 to 0.25 can be seen in Figure S4. According to the classification of the International Union of Pure and Applied Chemistry (IUPAC), the adsorption-desorption isotherms of the catalyst materials belonged to type IV, with a typical hysteresis loop of the H3 type [19,20], caused by the capillary condensation of mesoporous structures. The data for the specific surface area and pore volume are given in Table 1. Pure Fe_2O_3 was found to have a specific surface area of only $4 \text{ m}^2 \cdot \text{g}^{-1}$ and a pore volume of only $0.11 \text{ cm}^3 \cdot \text{g}^{-1}$. Fe_2O_3 is similarly porous, but has an almost nil pore diameter, suggesting large amounts of accumulated Fe_2O_3 particles. On the other hand, compared to pure Fe_2O_3 , the KCC-1 carrier exhibits a significantly larger specific surface area of $645 \text{ m}^2 \cdot \text{g}^{-1}$ and a pore volume of $1.93 \text{ cm}^3 \cdot \text{g}^{-1}$. When doped with FeO_x NPs, $x\%\text{Fe@KCC-1}$ showed lower specific surface areas, pore volumes, and pore sizes than their non-doped counterparts. In particular, the specific surface area of $x\%\text{Fe@KCC-1}$ ($x = 0, 1, 3, 5, 7$ and 10) catalysts decreased from $645 \text{ m}^2 \cdot \text{g}^{-1}$ to $397 \text{ m}^2 \cdot \text{g}^{-1}$ and the pore volume decreased from $1.52 \text{ cm}^3 \cdot \text{g}^{-1}$ to $0.67 \text{ cm}^3 \cdot \text{g}^{-1}$ when the loading of the active component of FeO_x NPs was increased from 1% to 10%. However, the pore size of FeKCC-1 remained basically unchanged at about 3.1 nm, which means that the pore structure of KCC-1 was not disrupted after introducing FeO_x . Pore size distribution analysis of $x\%\text{Fe@KCC-1}$ showed that mesopores 3.1 nm in size were embedded in the floral fiber microspheres of KCC-1 molecular sieves.

Table 1. Structural parameters for $x\%\text{Fe@KCC-1}$ ($x = 0, 1, 3, 5, 7$ and 10) and related materials.

Catalysts	Specific Surface Area ($\text{m}^2 \cdot \text{g}^{-1}$) ^a	Pore Volume ($\text{cm}^3 \cdot \text{g}^{-1}$) ^b	Pore Sizes (nm) ^b
KCC-1	645	1.68	3.1
Fe_2O_3	4	0.11	31.7
1%Fe@KCC-1	576	1.52	3.1
3%Fe@KCC-1	550	1.45	3.1
5%Fe@KCC-1	520	1.33	3.1
7%Fe@KCC-1	479	1.21	3.1
10%Fe@KCC-1	397	0.67	3.1

^a: Calculated from the linear part of the BET formula ($P/P_0 = 0.05\text{--}0.25$). ^b: Calculated from the BJH Equation.

The reducibility of $x\%\text{Fe@KCC-1}$ ($x = 0, 1, 3, 5, 7$ and 10) catalysts was investigated using H_2 -TPR (Figure 2). There were three reduction peaks of Fe_2O_3 with relatively large peak areas at 392 °C, 602 °C, and 754 °C, respectively. The first peak at 392 °C was attributed to the reduction of Fe_2O_3 to Fe_3O_4 , the peak at 602 °C was owed to the reduction of Fe_3O_4 to FeO, and the peak at 754 °C was attributed to the reduction of FeO to metal Fe. Overall, the total reduction process was: $\text{Fe}_2\text{O}_3 \rightarrow \text{Fe}_3\text{O}_4 \rightarrow \text{FeO} \rightarrow \text{Fe}$. There was also a redox cycle of $\text{Fe}^{3+} \leftrightarrow \text{Fe}^{2+} \leftrightarrow \text{Fe}$ [21,22]. As Fe was introduced, the temperatures corresponding to all the reduction processes remained almost unchanged. In addition, as the Fe content increased from 5% to 10%, the areas of the three reduction peaks gradually increased, indicating that the number of active oxygen species increased, which was favorable for CO catalytic elimination [18].

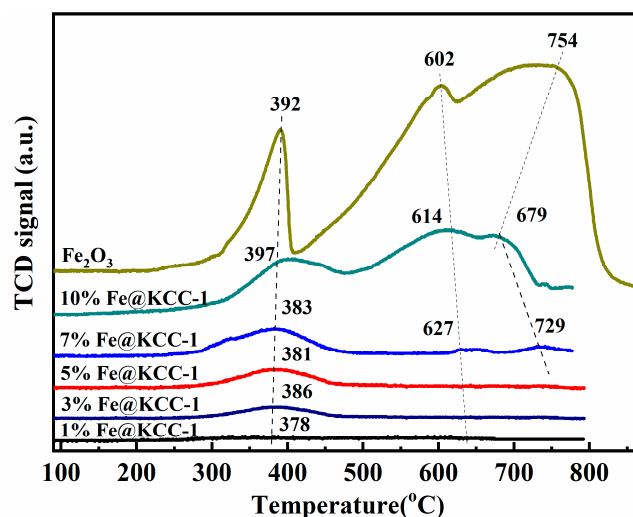


Figure 2. The H₂-TPR of x%Fe@KCC-1 (x = 0, 1, 3, 5, 7 and 10) and related catalyst materials.

2.2. Catalytic Activity Assessment

The CO catalytic activities of x%Fe@KCC-1 (x = 0, 1, 3, 5, 7 and 10) and related catalyst materials were evaluated, and the obtained results are displayed in Figure 3. Pure KCC-1 support showed negligible catalytic activity for CO oxidation under experimental conditions. After loading the x%Fe active component on the KCC-1 support, the CO conversion improved drastically. The x%Fe@KCC-1 (x = 0, 1, 3, 5, 7 and 10) catalysts exhibited better CO catalytic activity, and the following total CO conversion temperatures were obtained: 7%Fe@KCC-1 (158 °C) > 10%Fe@KCC-1 (197 °C) > 5%Fe@KCC-1 (218 °C) > 3%Fe@KCC-1 (239 °C) > 1%Fe@KCC-1 (298 °C). These results suggest that the morphological structure of the floral fiber microspheres is conducive to the gas-solid heterogeneous catalytic oxidation reaction. It is noteworthy that the CO conversion of 10%Fe@KCC-1 is slightly lower than that of 7%Fe@KCC-1, which can be attributed to the higher content of the active component leading to its aggregation on the surface of KCC-1, resulting in a reduction of exposed Fe active sites, which is also observed in other reported catalysts [23,24]. The temperature-dependent reaction was calculated to estimate the apparent activation energy of the x%Fe@KCC-1 (x = 0, 1, 3, 5, 7 and 10) catalysts, and the CO conversion shown in Figure S5 was <20% to avoid diffusion limitations. Assuming that the combustion of CO in the presence of excess oxygen obeys a first-order reaction mechanism with respect to CO concentration (c): $r = -kc = (-A \exp(-E_A/RT))c$, where r, k, A, and E_A are the reaction rate (mol·s⁻¹), rate constant (s⁻¹), pre-exponential factor, and apparent activation energy (kJ·mol⁻¹) [25,26], respectively. Arrhenius plots of different catalysts with CO conversion at <20% and GHSV at 960,000 h⁻¹ are shown in Figure S5. As calculated, the E_A values of the four catalysts are, in order: 7%Fe@KCC-1 < 10%Fe@KCC-1 < 5%Fe@KCC-1 < 3%Fe@KCC-1, in which the 7%Fe@KCC-1 catalyst has the lowest E_A value (96.2 kJ·mol⁻¹), indicating that the prepared x%Fe@KCC-1 catalysts have excellent CO oxidation ability.

2.3. Adsorption of CO and O₂ on Fe₂O₃ (001) Catalyst Surface

The optimized structure of the Fe₂O₃ (001) catalyst (Figure S6) revealed that the Fe₂O₃ (001) surfaces exhibited two potential adsorption sites (Fe-top and O-top), with advantageous compositional alterations and reconstructions [27]. To simulate these surfaces, a vacuum gap of 20 Å was introduced in the Z direction. According to the calculation results, Fe and O atoms on the surface of the modeled structures are most likely to be the adsorption sites for CO and O₂ gas molecules. Therefore, the use of non-precious metal oxides (Fe₂O₃) in the catalytic oxidation of CO is a design principle for the development of advanced catalytic systems with a wide range of applications.

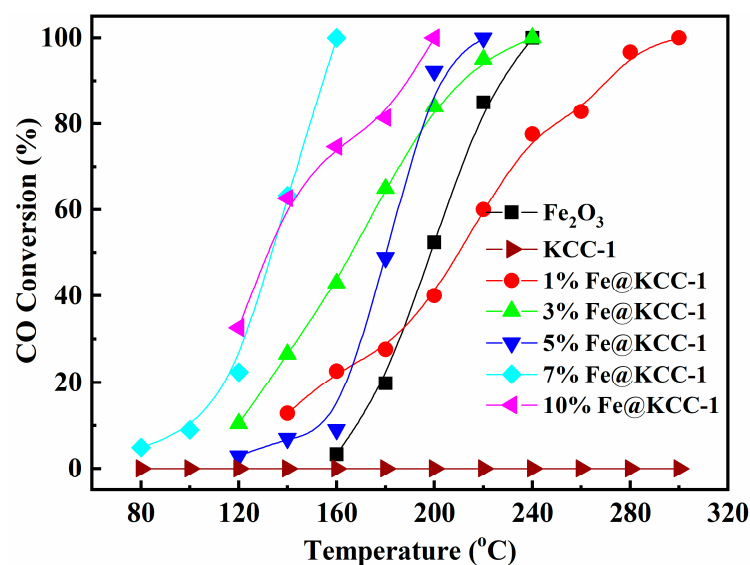


Figure 3. Catalytic performance of $x\%Fe@KCC-1$ and related catalyst materials. Reaction conditions: 1% CO, 21% O₂, balanced by N₂, and WHSV = 18,000 mL·g_{cat.}⁻¹·h⁻¹.

The adsorption of reaction (CO and O₂) gas molecules on a catalyst's surface is a crucial step in the removal of CO from industrial exhaust. Therefore, single-adsorption and co-adsorption of these two gas molecules on the catalyst surface were separately investigated using density functional theory (DFT) calculations based on the optimized Fe₂O₃ (001) catalyst structure (Figure 4). The gas molecules were placed 3.5 Å above the Fe₂O₃ (001) surface, and then the structures were optimized. Figure 4a,b show the optimized single-adsorption configuration and projected density of states (PDOS) of O₂ and CO gas molecules on the Fe₂O₃ (001) catalyst's surface, respectively. CO and O₂ gas molecules tended to selectively adsorb only on the Fe-top site. As shown in Figure 4a, the formed Fe–C bond length was 1.845 Å, with an adsorption energy of –2.70 eV. In Figure 4b, O₂ was the most important reactant in the catalytic reaction. The formed Fe–O bond length was 1.847 Å, with an adsorption energy of –2.91 eV on the Fe₂O₃ (001) catalyst surface, which exhibited bridging adsorption. According to the PDOS results, the highest occupied molecular orbitals of O₂ hybridize with the lowest unoccupied molecular orbitals of Fe on the catalyst's surface in the adsorption configurations of CO and O₂. To further research the adsorption behavior of CO and O₂ gas molecules on Fe₂O₃ (001) surface, their co-adsorption on the catalyst's surface was also studied via DFT calculations. The newly formed Fe–C and Fe–O bond lengths were 1.913 Å and 1.832 Å, respectively, with E_{ads} of –3.25 eV. The analysis of the PDOS results demonstrated that the adsorption of these reactive gas molecules on the Fe₂O₃ (110) surface all involved chemisorption, which indicated that they could be well activated by the catalyst surface. Therefore, carbon monoxide was efficiently converted on the Fe₂O₃ (110) catalyst surface.

2.4. Analysis of Reaction Transient Intermediates on Catalyst Surfaces

In order to study the transient intermediates of the CO catalytic removal reaction on the surface of the 7%Fe@KCC-1 catalyst more deeply, CO + O₂ transient adsorption experiments were carried out at 200 °C, and the detected results are presented in Figure 5. The peaks near 2119 cm⁻¹ and 2174 cm⁻¹ are attributed to CO species linearly adsorbed on the surface Fe³⁺ sites (Fe³⁺-CO) [28]. These results indicate that CO can be readily adsorbed on the surface active sites of the 7%Fe@KCC-1 catalyst, where it formed reactive intermediates. As O₂ was introduced into the system, these two peaks, corresponding to adsorbed state species of CO, disappeared rapidly. This suggests that the O₂ adsorption activation capacity of $x\%Fe@KCC-1$ catalysts may be stronger than that for CO, which strongly supports the DFT calculations results (Figure 4). Species found on the surface of

the 7%Fe@KCC-1 catalyst indicate that the catalytic oxidation of CO mainly follows the Langmuir-Hinshelwood (L-H) and/or Eley-Rideal (E-R) mechanisms [29].

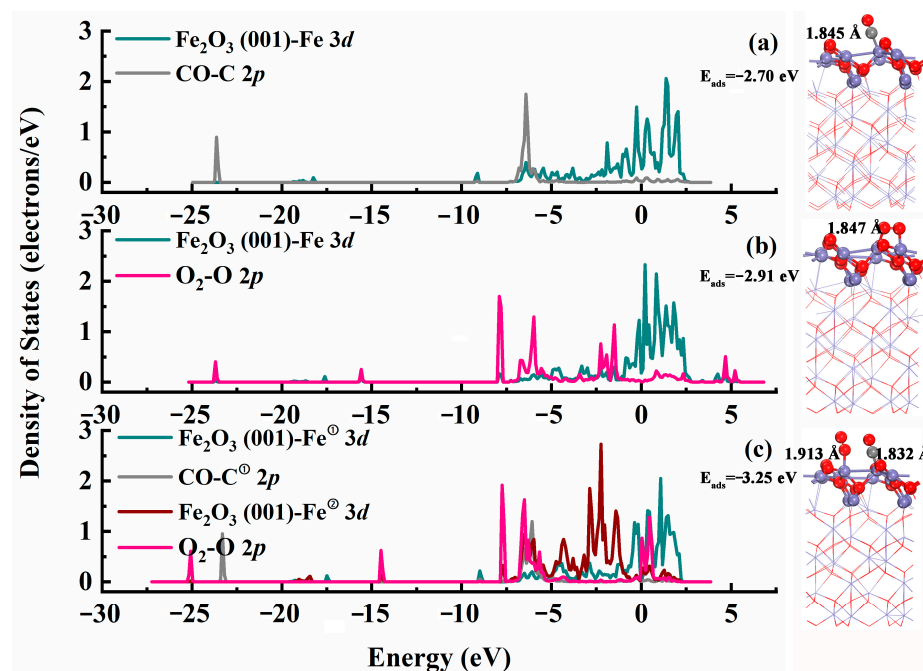


Figure 4. The optimized (a,b) single-molecule adsorption and (c) double-molecule adsorption configurations and PDOS on Fe_2O_3 (001) catalyst surface for O_2 and CO gas molecules, respectively.

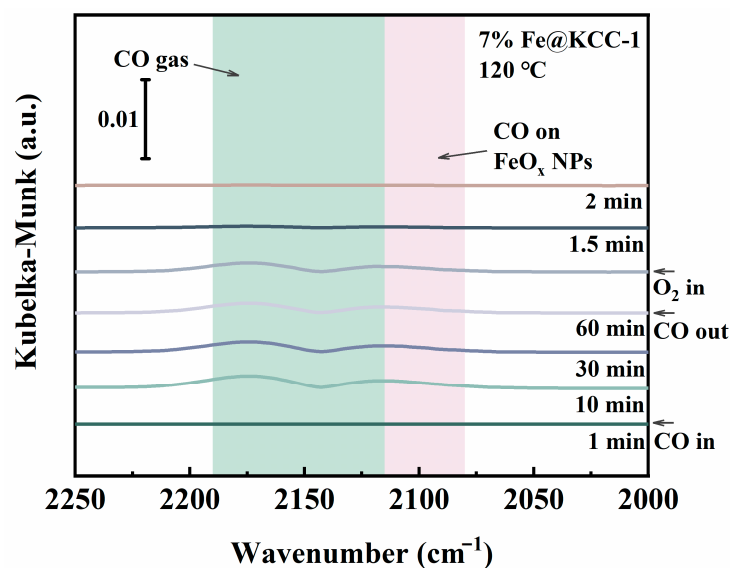


Figure 5. In-situ DRIFTS versus time curves for transient reactions of 5% O_2 ($30 \text{ mL}\cdot\text{min}^{-1}$) and pre-adsorbed CO/ N_2 species over 7% Fe@KCC-1 catalyst at $120 \text{ }^\circ\text{C}$ for 60 min. (The background color is used to differentiate between species adsorbed on different surfaces.)

The catalytic oxidation mechanism of CO over the 7% Fe@KCC-1 catalyst under a dry reaction atmosphere ($\text{CO} + \text{O}_2$) was investigated using DFT calculations (Figure 6). Figure 5 shows the transient in-situ DRIFTS curves for CO + O_2 reactions over the 7% Fe@KCC-1 catalyst. The detailed analysis reaction path is: ① $\text{CO}_{\text{gas}} \rightarrow \text{CO}_{\text{ads}}$ and $\text{O}_{2\text{gas}} \rightarrow \text{O}_{2\text{ads}}$, ② $\text{CO}_{\text{ads}} + \text{O}_{2\text{ads}} \rightarrow \text{CO}_{2\text{free}} + \text{FeO}_{x+1}$, ③ $\text{FeO}_{x+1} + \text{CO}_{\text{ads}} \rightarrow \text{FeO}_x + \text{CO}_{2\text{ads}}$, and ④ $\text{CO}_{2\text{ads}} \rightarrow \text{CO}_{2\text{gas}}$. Doping Fe increased the CO catalytic oxidation activity of the 7% Fe@KCC-1 catalyst due to the formation of boundaries between KCC-1 and 7% FeO_x

species, which led to the rapid reaction of CO adsorbed on FeO_x nanoparticles with oxygen species provided by the $\text{Fe}^{2+} \leftrightarrow \text{Fe}^{3+}$ redox cycle. As exhibited in Figure 5, CO and O_2 were simultaneously adsorbed on 7%Fe@KCC-1 catalyst surface. Reaction gas molecules were first co-adsorbed on the 7%Fe@KCC-1 catalyst surface to form transient intermediates species (such as CO_{ads}). Adsorbed reaction gas molecules (CO and O_2) were activated and converted to CO_2 , which dissociated from the catalyst surface and formed a peroxide structure (FeO_{x+1}). The reaction energy (E_r) of this step was 2.68 eV, which may determine the overall rate of catalytic CO oxidation. Additional CO was adsorbed at the Fe sites on the catalyst surface and interacted with the generated perovskite structure to produce CO_2 . During this catalytic elimination process, the physicochemical properties of the catalyst remained unchanged before and after the elimination reaction. Thus, the FeO_{x-1} structure was recovered by oxidation of O_2 gas molecule ($\text{FeO}_{x-1} + \text{O}_{2\text{ads}} \rightarrow \text{FeO}_x + \text{O}_{\text{ads}}$). The CO catalytic oxidation on the 7%Fe@KCC-1 surface followed the E-R and L-H mechanisms. Adsorbed O_2 reacted with adsorbed or gaseous CO gas molecules to form $\text{CO}_{2\text{ads}}$ species. Subsequently, the $\text{CO}_{2\text{ads}}$ dissociated from the iron oxide (110) catalyst, and the catalyst was subsequently regenerated.

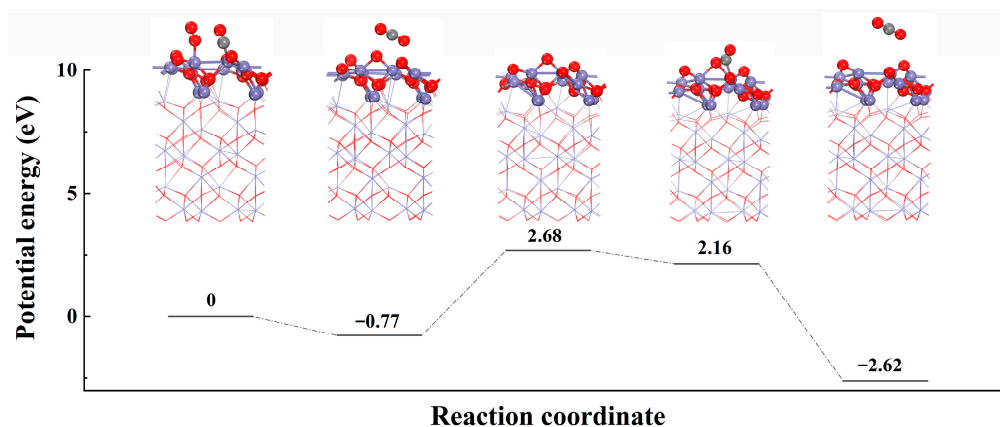


Figure 6. The CO removal pathway and energetic barrier on the Fe_2O_3 (110) catalyst face. (Red: O, Purple: Fe, Grey: C).

3. Conclusions

In this study, a mesoporous silica material, KCC-1, was synthesized and used as a support for the confinement of FeO_x nanoparticles (NPs). The performance of the $x\%\text{Fe@KCC-1}$ catalysts obtained for the catalytic oxidation of CO was systematically investigated. The experimental results showed that due to the carrier's large specific surface area and abundant mesopores, the FeO_x nanoparticles were widely dispersed on the KCC-1 support. The particle size of FeO_x was very small, resulting in excellent interactions between the FeO_x NP's active component and the KCC-1 carrier, which improved the CO catalytic oxidation on the catalyst's surface. Doping with Fe increased the CO catalytic oxidation activity of the 7% Fe@KCC-1 catalyst due to the formation of boundaries between KCC-1 and 7% FeO_x species, which led to the rapid reaction of CO adsorbed on FeO_x nanoparticles with oxygen species formed during the $\text{Fe}^{2+} \leftrightarrow \text{Fe}^{3+}$ redox cycle. FeO_x loading improved the CO adsorption capability of the catalyst, which facilitated the catalytic oxidation of CO, with the 7% FeO_x @KCC-1 catalyst achieving 100% CO conversion at 160 °C. A combination of in-situ DRIFTS and DFT calculations was used to establish the detailed catalytic CO removal pathway. The mechanism was as follows: ① $\text{CO}_{\text{gas}} \rightarrow \text{CO}_{\text{ads}}$ and $\text{O}_{2\text{gas}} \rightarrow \text{O}_{2\text{ads}}$, ② $\text{CO}_{\text{ads}} + \text{O}_{2\text{ads}} \rightarrow \text{CO}_{2\text{free}} + \text{FeO}_{x+1}$, ③ $\text{FeO}_{x+1} + \text{CO}_{\text{ads}} \rightarrow \text{FeO}_x + \text{CO}_{2\text{ads}}$, ④ $\text{CO}_{2\text{ads}} \rightarrow \text{CO}_{2\text{gas}}$. This study holds significance for further understanding the application potential of nano-catalysts in important oxidation reactions and provides valuable insights for the development of efficient CO oxidation catalysts.

4. Experimental Procedure

4.1. Catalyst Preparation

Chemicals: All chemicals were of analytical grade and were used as received without further purification. Cyclohexane (AR), *n*-pentanol (AR), tetraethyl orthosilicate (TEOS, AR), cetyltrimethylammonium bromide (CTAB, AR), urea (AR), acetone, ethanol, ethylene glycol, ammonia (25–28 wt.%, AR) and $\text{Fe}(\text{NO}_3)_3 \cdot 6\text{H}_2\text{O}$ (AR) were provided by Sinopharm Chemical Reagent Co., Ltd. (Beijing, China).

Synthesis of KCC-1: The KCC-1 support was made in compliance with previously reported methods [30]. In a typical procedure, 60.00 mL of cyclohexane, 3.00 mL of *n*-pentanol, and 5.00 g of TEOS were mixed to obtain Liquid A. Liquid B was created by dissolving 2.00 g of CTAB and 1.20 g of urea in 60 mL of deionized water. Then, Liquid B was gradually added to Liquid A. After being stirred for about 30 min, the resultant solution was put into a stainless steel autoclave and held at 120 °C for 6 h while being continuously stirred. The solid product was filtered and washed with acetone and anhydrous ethanol several times. Finally, the solids were dried in oven at 80 °C for 12 h and calcined at 550 °C (2 °C min⁻¹) for 6 h in air.

Synthesis of $x\%\text{Fe@KCC-1}$: The synthesis was performed in a beaker. In a typical procedure, 0.50 g of KCC-1 and an appropriate amount of $\text{Fe}(\text{NO}_3)_3 \cdot 6\text{H}_2\text{O}$ were dissolved in 10.00 mL of ethylene glycol. After being stirred for about 5 h, the resultant solid-liquid mixture was dried in a vacuum oven at 80 °C until the solvent completely evaporated. Finally, the solid was calcined in a tube furnace at 550 °C under N_2 and air atmosphere for 4 h and 2 h, respectively. The catalysts that generated were given the designation $x\%\text{Fe@KCC-1}$ ($x = 0, 1, 3, 5, 7, \text{ and } 10$), where x refers to the Fe mass loading.

Synthesis of Fe_2O_3 : A precipitation process was used to create Fe_2O_3 . In a typical procedure, a suitable quantity of $\text{Fe}(\text{NO}_3)_3 \cdot 6\text{H}_2\text{O}$ was dissolved in deionized water to give the final concentrations of 0.1 M. After being stirred for about 30 min, ammonia was added dropwise to the solution until the pH value equaled 10. For three hours, the mixture was agitated at 25 °C. The precipitate was filtered, washed, dried, and calcined using the procedure described above.

4.2. Evaluation of the Catalytic CO Oxidation Performance

All evaluation experiments of the catalysts for CO catalytic oxidation were measured in a continuous flow fixed-bed reactor. To evaluate the effectiveness of internal diffusion, the Weisz-Prater Criterion was utilized. The CO oxidation activity was assessed using the standard reaction conditions: 50 mg catalyst, 1 vol.% [CO], 21 vol.% [O₂], and N_2 as balance gas at a total flow rate of 30 mL min⁻¹. The reactants and products were collected and examined using an N-2000 workstation and a GC9310 gas chromatograph, which was outfitted with a TDX-01 column and a TCD detector. The conversion of CO (X_{CO}) was calculated using Equation (1):

$$X_{\text{CO}} = \left(1 - \frac{S_{\text{CO-outlet}}}{S_{\text{CO-inlet}}} \right) \times 100\% \quad (1)$$

where $S_{\text{CO-outlet}}$ and $S_{\text{CO-inlet}}$ are the CO concentrations in the inlet and outlet gas streams.

4.3. Catalyst Characterization

The samples were analyzed by XRD testing in the range of 10–80° (2 θ) using a Bruker D8 ADVANCE (Bruker, Karlsruhe, German) diffractometer. N_2 adsorption-desorption isotherms were measured by an automated analyzer (Micromeritics ASAP2460). SEM and transmission electron microscope (TEM) images were captured under a field GeminiSEM300 emission SEM (Zeiss, Jena, German) and a FEI-TALOS-F200X TEM (Thermo Fisher Scientific, Waltham, MA, USA), respectively.

An is50 spectrometer fitted with a Harrick Scientific DRIFTS catalyst sample cell and a liquid N_2 cooled mercury cadmium telluride A (MCT-A) detector was utilized to gather

in-situ DRIFT spectra. Prior to every test, every sample had a 60 min pretreatment at 400 °C with a 30 mL·min⁻¹ N₂ flow. After pretreatment in an N₂ environment, the background spectrum at the target temperature was obtained and deducted from the sample spectra for every measurement. After pretreatment, the catalysts were subjected to 1% CO/N₂ (30 mL·min⁻¹) and subjected to undergo adsorption at 120 °C for the in-situ transient reactions of pre-adsorbed CO. After an hour, the sample was exposed to a 21% O₂/N₂ (30 mL·min⁻¹), and the reaction was tracked over time.

4.4. DFT Calculations

For the DFT calculations, the Vienna Ab-initio Simulation Package (VASP) was utilized [31–33]. The solution to the Kohn-Sham equations was obtained using the projector augmented wave (PAW) method [34]. The generalized gradient approximation and the Perdew-Burke-Ernzerhof (GGA-PBE) exchange correlation function were employed. A dipole correction was incorporated to account for the total energy and suppress the dipole moment arising from the adsorption of metal atoms [35]. Thus, in this paper, $U = 4.0$ eV was employed for the d-orbitals of Fe, demonstrating excellent agreement with experimental data [27,36].

The adsorption energy (E_{ads}) and reaction energy (E_r) are shown in the Supplementary Materials.

Supplementary Materials: The following supporting information can be downloaded at: <https://www.mdpi.com/article/10.3390/catal14010063/s1>. Evaluation of the catalytic performance. Figure S1. (a,b) TEM, (c–f) HAADF-STEM and Mapping images of 7%Fe@KCC-1 catalysts. Figure S2. (a–d) HRTEM for reduced 7%Fe@KCC-1 catalyst by H₂. Figure S3 XRD patterns of $x\%$ Fe@KCC-1 ($x = 0, 1, 3, 5, 7$ and 10) and related catalyst materials. Figure S4. (a) N₂ adsorption–desorption isotherms and (b) pore size distribution curves of $x\%$ Fe@KCC-1 ($x = 0, 1, 3, 5, 7$ and 10) and related catalyst materials. Figure S5. Arrhenius plots for CO oxidation over different catalysts. Figure S6. Top and side view of the optimized Fe₂O₃ (001) catalyst structure.

Author Contributions: Conceptualization by G.L., W.F., Y.L. and J.Y.; supervision by H.P.; writing—original draft by G.L., Y.L. and W.F.; writing—review and editing by S.Z., W.L., Y.C., Y.W. and H.P.; methodology by G.L., H.P. and S.Z. All authors have read and agreed to the published version of the manuscript.

Funding: This work was supported by the National Natural Science Foundation of China (22276076, 21976078 and 22306086), the Natural Science Foundation of Jiangxi Province (20202ACB213001, 20232BCJ22003 and 20232BAB213028), the National Engineering Laboratory for Mobile Source Emission Control Technology (NELMS2019A12), the State Key Laboratory of Clean Energy Utilization (ZJUCEU2022015), and the Natural Science Foundation of Chongqing (CSTB2023NSCQ-MSX0950), all of which are greatly acknowledged by the authors.

Data Availability Statement: The data are contained within the article.

Conflicts of Interest: The authors declare no conflicts of interest.

References

1. Theis, J.; Ura, J.; Getsoian, A.; Prikhodko, V.; Thomas, C.; Pihl, J.; Lardinois, T.; Gounder, M.; Wei, X.; Ji, Y.; et al. Effect of framework Al pairing on NO storage properties of Pd-CHA passive NO_x adsorbers. *Appl. Catal. B Environ.* **2023**, *322*, 122074. [CrossRef]
2. Kamal, M.; Razzak, A.; Hossain, M. Catalytic oxidation of volatile organic compounds (VOCs)—A review. *Atmos. Environ.* **2016**, *140*, 117–134. [CrossRef]
3. Chen, S.; Xie, R.; Liu, Z.; Ma, L.; Yan, N. Efficient NO_x Reduction against Alkali Poisoning over a Self-Protection Armor by Fabricating Surface Ce₂(SO₄)₃ Species: Comparison to Commercial Vanadia Catalysts. *Environ. Sci. Technol.* **2023**, *57*, 2949–2957. [CrossRef]
4. Oboudatian, H.; Safaei-Ghomi, J. Silica nanospheres KCC-1 as a good catalyst for the preparation of 2-amino-4H-chromenes by ultrasonic irradiation. *Sci. Rep.* **2022**, *12*, 2381. [CrossRef]
5. Palanichamy, K.; Umasankar, S.; Ganesh, S.; Sasirekha, N. Highly coke resistant Ni–Co/KCC-1 catalysts for dry reforming of methane. *Int. J. Hydrogen Energy* **2023**, *48*, 11727–11745. [CrossRef]

6. Oboudatian, H.; Safaei-Ghomi, J. Fibrous nanosilica spheres KCC-1@NH₂ as highly effective and easily retrievable catalyst for the synthesis of chromenes. *Res. Chem. Intermediat.* **2022**, *48*, 2069–2085. [[CrossRef](#)]
7. Li, G.B.; Zhang, Y.Y.; Yan, J.; Luo, Y.W.; Wang, C.C.; Feng, W.W.; Zhang, S.; Liu, W.; Zhang, Z.; Peng, H.G. Insights into SnO₂ nanoparticles supported on fibrous mesoporous silica for CO catalytic oxidation. *Catalysts* **2023**, *13*, 1156. [[CrossRef](#)]
8. Xiang, G.H.; Zhao, S.; Wei, C.D.; Liu, C.Y.; Fei, H.L.; Liu, Z.G.; Yin, S.F. Atomically dispersed Au catalysts for preferential oxidation of CO in H₂-rich stream. *Appl. Catal. B Environ.* **2021**, *296*, 120385–120396. [[CrossRef](#)]
9. Xin, Y.; Zhang, N.N.; Lv, Y.N.; Wang, J.; Li, Q.; Zhang, Z.L. Room-Temperature CO oxidative coupling for oxamide production over in-terfacial Au/ZnO catalysts. *ACS Catal.* **2023**, *13*, 735–743.
10. Huang, R.; Kin, K.; Kim, H.J.; Jang, M.J.; Han, J.W. Size-Controlled Pd nanoparticles loaded on Co₃O₄ nanoparticles by calcination for enhanced CO oxidation. *ACS Appl. Nano Mater.* **2020**, *3*, 486–495. [[CrossRef](#)]
11. Liu, Y.; Yang, F.; Ning, Y.; Liu, Q.; Zhang, Y.; Chen, H.; Bao, X. CO adsorption on a Pt (111) surface partially covered with FeO_x nanostructures. *J. Energy Chem.* **2017**, *26*, 602–607. [[CrossRef](#)]
12. Bai, Z.; Wang, J.; Yang, Q. Iron doped fibrous-structured silica nanospheres as efficient catalyst for catalytic ozonation of sulfamethazine. *Environ. Sci. Pollut. Res. Int.* **2018**, *25*, 10090–10101. [[CrossRef](#)]
13. Cai, W.; Zhong, Q.; Zhao, W.; Bu, Y. Focus on the modified Ce_xZr_{1-x}O₂ with the rigid benzene-multi-carboxylate ligands and its catalysis in oxidation of NO. *Appl. Catal. B Environ.* **2014**, *158–159*, 258–268. [[CrossRef](#)]
14. Liu, D.; Quek, X.Y.; Cheo, W.N.E.; Lau, R.; Borgna, A.; Yang, Y. MCM-41 supported nickel-based bimetallic catalysts with superior stability during carbon dioxide reforming of methane: Effect of strong metal–support interaction. *J. Catal.* **2009**, *266*, 380–390. [[CrossRef](#)]
15. Dadras, J.; Jimenez-Izal, E.; Alexandrova, A.N. Alloying Pt Sub-nano-clusters with boron: Sintering preventative and coke antagonist. *ACS Catal.* **2015**, *5*, 5719–5727. [[CrossRef](#)]
16. Zhang, X.H.; Zhang, L.; Peng, H.G.; You, X.; Peng, C.; Xu, X.; Liu, W.M.; Fang, X.; Wang, Z.; Zhang, N.; et al. Nickel nanoparticles embedded in mesopores of AISBA-15 with a perfect peasecod-like structure: A catalyst with superior sintering resistance and hydrothermal stability for methane dry reforming. *Appl. Catal. B Environ.* **2018**, *224*, 488–499. [[CrossRef](#)]
17. Synowiec, M.; Zákutná, D.; Trenczek-Zajac, A.; Radecka, M. The impact of nanometric Fe₂O₃ on the magnetic, electronic, and photocatalytic behavior of TiO₂@Fe₂O₃ heterostructures. *Appl. Surf. Sci.* **2023**, *608*, 155186. [[CrossRef](#)]
18. Peng, H.G.; Zhang, X.H.; Han, X.; You, X.; Lin, S.; Chen, H.; Liu, W.; Wang, X.; Zhang, N.; Wang, Z.; et al. Catalysts in coronas: A surface spatial confinement strategy for High-Performance catalysts in methane dry reforming. *ACS Catal.* **2019**, *9*, 9072–9080. [[CrossRef](#)]
19. Bratan, V.; Munteanu, C.; Hornoiu, C.; Vasile, A.; Papa, F.; State, R.; Preda, S.; Culita, D.; Ionescu, N. CO oxidation over Pd supported catalysts—In situ study of the electric and catalytic properties. *Appl. Catal. B Environ.* **2017**, *207*, 166–173. [[CrossRef](#)]
20. Zhang, G.; Han, W.; Zhao, H.; Zong, L.; Tang, Z. Solvothermal synthesis of well-designed ceria-tin-titanium catalysts with enhanced catalytic performance for wide temperature NH₃-SCR reaction. *Appl. Catal. B Environ.* **2018**, *226*, 117–126. [[CrossRef](#)]
21. Jeong, M.; Lee, D.; Bae, W. Reduction and oxidation kinetics of different phases of iron oxides. *Int. J. Hydrogen Energy* **2015**, *40*, 2613–2620. [[CrossRef](#)]
22. Meshkani, F.; Rezaei, M. Preparation of mesoporous nanocrystalline alkali promoted chromium free catalysts (Fe₂O₃–Al₂O₃–NiO) for a high temperature water gas shift reaction. *RSC Adv.* **2015**, *5*, 9955–9964. [[CrossRef](#)]
23. Feng, B.; Shi, M.; Liu, J.; Han, X.; Lan, Z.; Gu, H.; Wang, X.; Sun, H.; Zhang, Q.; Li, H.; et al. An efficient defect engineering strategy to enhance catalytic performances of Co₃O₄ nanorods for CO oxidation. *J. Hazard. Mater.* **2020**, *394*, 122540. [[CrossRef](#)]
24. Wang, Y.; Liu, C.; Liao, X.; Liu, Y.; Hou, J.; Pham-Huu, C. Enhancing oxygen activation on high surface area Pd-SnO₂ solid solution with isolated metal site catalysts for catalytic CH₄ combustion. *Appl. Surf. Sci.* **2021**, *564*, 150368. [[CrossRef](#)]
25. Jiang, H.Y.; Dai, H.X.; Meng, X.; Zhang, L.; Au, C.T. Hydrothermal fabrication and visible-light-driven photocatalytic properties of bismuth vanadate with multiple morphologies and/or porous structures for Methyl Orange degradation. *J. Environ. Sci.* **2012**, *24*, 449–457. [[CrossRef](#)]
26. Liu, Z.M.; Zhang, S.X.; Li, J.H.; Zhu, J.Z.; Ma, L.L. Novel V₂O₅-CeO₂/TiO₂ catalyst with low vanadium loading for the selective catalytic reduction of NO_x by NH₃. *Appl. Catal. B Environ.* **2014**, *158*, 11–19. [[CrossRef](#)]
27. Fang, Q.; Zhu, B.; Sun, Y.; Zhu, Z.; Xu, M.; Ge, T. Mechanistic insight into the selective catalytic reduction of NO by NH₃ over α-Fe₂O₃ (001): A density functional theory study. *Catal. Sci. Technol.* **2019**, *9*, 116–124. [[CrossRef](#)]
28. Duan, H.; Zeng, W.; Tang, X.; Yu, B.; Chen, S.; Lian, X. Theoretical investigation for the reaction of CO oxidation by N₂O on Fe₆M (M = Fe, Co, Ni, Mn) clusters. *React. Kinet. Mech. Catal.* **2022**, *135*, 3021–3030. [[CrossRef](#)]
29. Feng, C.; Liu, X.; Zhu, T.; Tian, M. Catalytic oxidation of CO on noble metal-based catalysts. *Environ. Sci. Pollut. Res.* **2021**, *28*, 24847–24871. [[CrossRef](#)]
30. Li, Y.L.; Ying, J.W.; He, T.Y.; Li, G.B.; Zhang, H.X.; Huang, S.; Huang, T.; Liu, W.M.; Peng, H.G. Ultra-small Pt-Ni bimetallic nanoparticles confined in dendritic mesoporous silica with remarkable CO catalytic oxidation performance. *Ind. Eng. Chem. Res.* **2023**, *62*, 9159–9168. [[CrossRef](#)]
31. Kohn, W.; Sham, L.J. Self-Consistent equations including exchange and correlation effects. *Phys. Rev. B Condens. Matter.* **1965**, *140*, 1133–1138. [[CrossRef](#)]
32. Dong, W.; Kresse, G.; Furthmüller, J.; Hafner, J. Chemisorption of H on Pd (111): An ab initio approach with ultrasoft pseudopotentials. *Phys. Rev. B Condens. Matter.* **1996**, *54*, 2157–2166. [[CrossRef](#)]

33. Kresse, G.; Furthmüller, J. Efficiency of Ab-initio total energy calculations for metals and semiconductors using a plane-wave basis set. *Comp. Mater. Sci.* **1996**, *6*, 15–50. [[CrossRef](#)]
34. Hammer, B.; Hansen, L.B.; NoRskov, J.K. Improved adsorption energetics within density-functional theory using revised Perdew-Burke-Ernzerhof functionals. *Phys. Rev. B Condens. Matter.* **1999**, *59*, 7413–7421. [[CrossRef](#)]
35. Perdew, J.P.; Burke, K.; Ernzerhof, M. Generalized gradient approximation made simple. *Phys. Rev. Lett.* **1996**, *77*, 3865–3868. [[CrossRef](#)]
36. Neugebauer, J.; Scheffler, M. Adsorbate-substrate and adsorbate-adsorbate interactions of Na and K adlayers on Al (111). *Phys. Rev. B Condens. Matter.* **1992**, *46*, 16067–16080. [[CrossRef](#)]

Disclaimer/Publisher’s Note: The statements, opinions and data contained in all publications are solely those of the individual author(s) and contributor(s) and not of MDPI and/or the editor(s). MDPI and/or the editor(s) disclaim responsibility for any injury to people or property resulting from any ideas, methods, instructions or products referred to in the content.